Bioinspired Carbonized Polymer Microspheres for Full-Color Whispering Gallery Mode Emission for White Light Emission, Unclonable Anti-Counterfeiting, and Chemical Sensing Applications

Barun Kumar Barman, * *David Hernández-Pinilla, Thang Duy Dao, Kenzo Deguchi, Shinobu Ohki, Kenjiro Hashi, Atsushi Goto, Tsuyoshi Miyazaki, Karuna Kar Nanda, and Tadaaki Nagao**

Keywords: Carbonized polymer microsphere, solid-state fluorescence, whispering gallery mode, energy transfer, white-light emission, anti-counterfeiting

Light-element-based fluorescent materials, colloidal graphene quantum dots, and carbon dots (CDs) have sparked immense scientific interest in the past decade. However, a significant challenge in practical applications has emerged concerning the development of solid-state fluorescence (SSF) materials. This study addresses this knowledge gap by exploring the unexplored photonic facets of C-based solid-state micro-photonic emitters. The proposed synthesis approach focuses on carbonized polymer microspheres (CPMs) instead of the conventional nanodots. These microspheres exhibit remarkable SSF spanning the entire visible spectrum, from blue to red. The highly spherical shape of CPMs imparts inbuilt photonic properties in addition to its intrinsic CD-based attributes. Leveraging their excitation-dependent photoluminescence property, these microspheres exhibit amplified spontaneous emission assisted by the whispering gallery mode (WGM) resonance across the visible spectral region. Remarkably, unlike conventional semiconductor quantum dots or dye-doped micro-resonators, this single microstructure showcases adaptable resonant emission without structural/chemical modifications. This distinctive attribute enables a plethora of applications, including microcavity-assisted energy transfer for white light emission, highly sensitive chemical sensing, and secure encrypted anti-counterfeiting measures. This interdisciplinary approach, integrating photonics and chemistry, provides a robust solution for light-element-based SSF with inherent photonic functionality and wide-ranging applications.

1. Introduction

Fluorescent carbon dots/carbonized polymer dots (CDs/CPDs) can be easily fabricated and exhibit unique luminescence in the visible to near-infrared wavelength region. These novel nanomaterials have garnered significant attention owing to their unique optical properties, photostability, low cost, and low toxicity, thus being utilized in widespread applications in various fields including optoelectronic devices, bioimaging, and catalysis.[1-6] Owing to the limitations of rare-earth elements and heavy toxic effects of chalcogenides and perovskite quantum dots on the environment and biological systems, researchers have started focusing on CDs/CPDs to overcome the drawbacks of conventional phosphor materials. However, the luminescence mechanism of these materials is ambiguous and controversial. Some hypotheses regarding the photoluminescence (PL) mechanisms of colloidal CDs/CPDs involving the C core, surface/edge, and molecular states have been reported based on both experimental and theoretical investigations.[7-11] However, the optical properties of CDs are still not fully understood because of their complex structures. CDs can be considered as fluorescent cocktails composed of multiple emission centers that arise from various molecular fluorophores (MFs) or their agglomerates.[12-15] Currently, significant focus is placed on advancing the synthesis of CD solutions with a high PL quantum yields (QYs), spanning from blue to red emission.[16-20] However, the practical application of CDs in lighting devices faces a challenge in transforming them into solid form, primarily due to aggregation-induced quenching (AIQ) resulting from excessive resonance energy transfer or direct π-π interactions between adjacent van der Waals forces in layers.[21-24] To overcome these limitations, a common practice involves integrating CDs into suitable host matrices such as organic polymers, starch, inorganic salts, and silica xerogel.[25, 26] Nevertheless, this blending approach encounters challenges such as poor photostability, uneven dispersion, and low QYs. Consequently, a pressing need exists for a systematic method of achieving self-quenching-resistant solid-state fluorescence characteristics by effectively curbing π-π stacking interactions and mitigating excessive Förster resonance energy transfer (FRET) of CDs in bulk or powder form without introducing external substances. Various research groups are actively pursuing the development of self-quenching-resistant solid-state CDs through a structural design strategy, demonstrating near-infrared (NIR)/red/green/blue solid-state FL C nanostructures. Consequently, a nanostructure design that hinders the energy transfer between the luminescent center could be an effective means of overcoming AIQ.[27, 28]

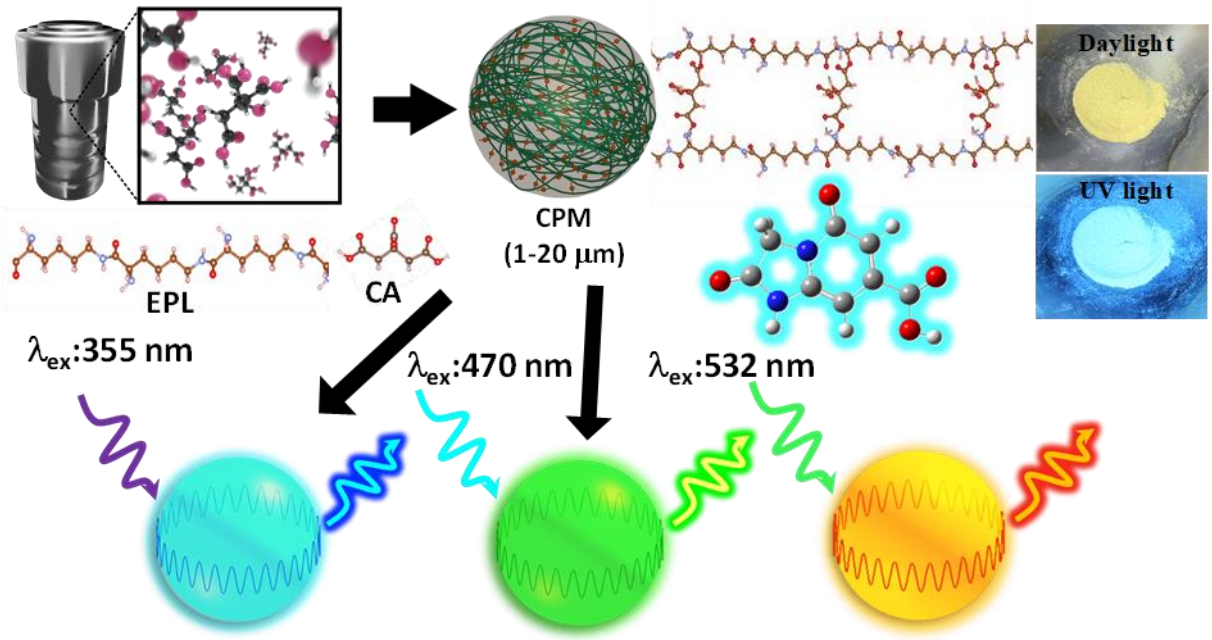

Figure 1. Schematic of the synthesis of CPM via hydrothermal reaction between CA and peptide structures and excitation-wavelength-dependent color variable photonic micro-resonator structure. The inset shows digital photographs of CPM under daylight and UV light.

Although CDs have been employed in several applications, their inbuilt photonic behavior remains unexplored. The dimensions of the material, particularly its shape and size, play a crucial role in determining its optical properties, such as scattering, reflection, and light confinement.[29-33] Furthermore, when microstructures adopt a highly spherical shape, strong photonic effects may emerge alongside the intrinsic CD-based properties.

Considering the barriers to solid-state light emission and the lack of desired photonics behaviors, we pioneered the creation of CPMs through MFs within microspheres, in contrast to traditional nanodot synthesis (schematic representation in **Figure 1**). This article reports the synthesis of novel photonic microstructures with matrix-embedded carbonized luminescent centers by adopting a transparent polymer as the starting material. The creation of CPMs on the gram scale involves microscopic phase separation through natural peptide crosslinking during hydrothermal processing. The microstructure exhibits solid-state light emission across the blue to red spectral range. Furthermore, as the microstructures have highly spherical shapes, CPMs show inbuilt "photonic functionality" emerging alongside intrinsic CD-based properties. By leveraging its excitation-wavelength-dependent PL, unlike typical inorganic semiconductor-based/dye-doped microresonators, a single CPM exhibits adjustable sharp whispering gallery

mode (WGM) resonances across a broader spectrum by altering the excitation source and successfully tailors and demonstrates color variable resonant emission without any structural alteration, in contrast to conventional semiconductor quantum dots/dye-doped microresonators.[32, 34, 35] This article establishes guidelines for the formation of CPM and its variants and reveals its internal structure from the microscale to the nanoscale, the nature of the emission center, and the light–matter interaction in the microcavities. These findings may help promote the development of technology in lighting, bioimaging, and sensing applications in the near future.

The conceptual novelty of this work includes several innovative aspects beyond CDs. (1) A rationally tunable hydrothermal/microwave synthesis method was established for the synthesis of CPMs with high sphericity. (2) Chromaticity-tunable emission (including direct white-light emission (WLE) was achieved using a single-object CPM. (3) The resultant microspheres were integrated with emission centers well separated by the polymeric chain matrix inside the microstructures, leading to the suppression of AIQ and yielding direct solid-state emission throughout the visible region. (4) The CPMs acted as a WGM microresonator and displayed ASE (quality (Q)-factors up to 1.6×10^3) throughout the visible wavelength region from blue to red depending on the excitation wavelength. Utilizing the excellent emission properties of these CPMs, we demonstrated efficient UV light harvesting, chromaticity-tunable WLE, multilevel authentication for hierarchically protected anti-counterfeit applications, and single-microparticle-based chemical sensing.

2. Results and Discussion

Proteins and peptides undergo denaturation when exposed to external stimuli, resulting in uncoiling and tangling of their structures. This process forms a mesh-like structure that traps the surrounding water by exposing the hydrophobic groups, leading to a loss of the solubility and color of the peptides (**Figure S1**).[36] By mimicking this biological process, a facile and single-step approach has been demonstrated for the gram-scale synthesis of a CPM structure using the cationic peptide, ε-polylysine (EPL), and citric acid (CA). Generally, CA and organic amines/polymers produce luminescent CDs/CPDs. Instead of organic amines, we used EPL possessing a natural cationic peptide structure. During the hydrothermal/microwave reaction, the peptides lose their original structure (α-helix, β-sheet, or random coil) through external stimuli (CA, pressure, or temperature), resulting in phase separation followed by morphological transformation into CPM by amide bond formation between the -COOH groups of CA and the NH_2 group of EPL.

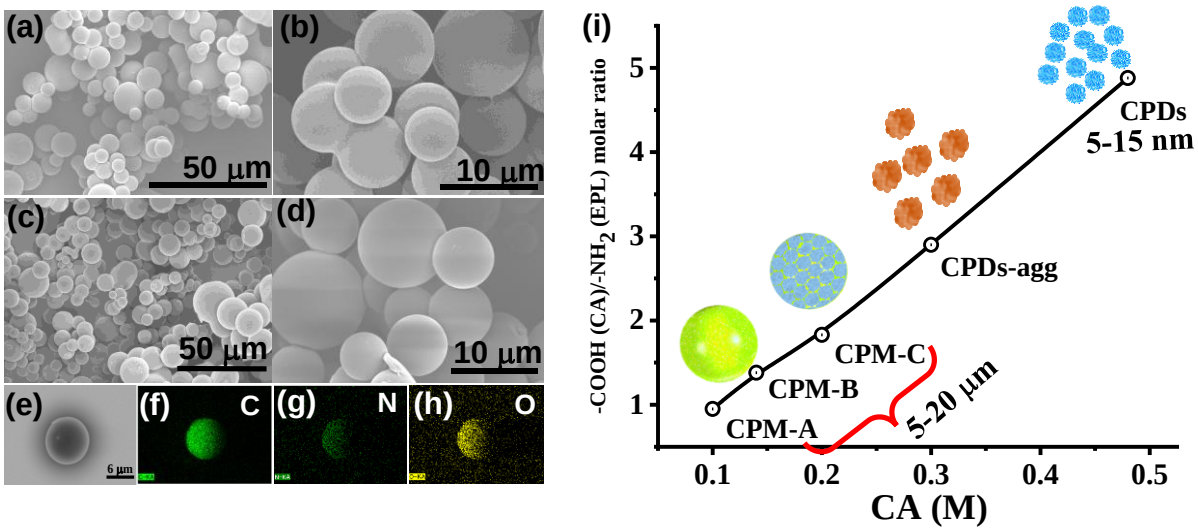

Figure 2. (a-d) SEM images of the CPMs (annotated as CPM-A and CPM-B). (e–h) SEM-EDS elemental mapping of a single CPM-A. (i) Synthesis strategy for the formation of CPMs into CPD structures by tuning the particle morphology via controlling the crosslinking.

Figure 1 shows a schematic representation of the formation of CPMs via facile, single-step hydrothermal/microwave synthesis. The hydrophobicity of the CPMs is due to the amino acid side chains that are natively crosslinked by the acid groups in CA, leading to an aggregated microstructure caused by exposing the hydrophobic peptide backbone. In situ optical photographs recorded during the microwave synthesis reaction also confirmed this crosslinking and phase separation from the solution and formation of CPMs (**Figure S2**). Briefly, an aqueous solution of EPL and CA underwent a hydrothermal/microwave reaction, and a yellow precipitate was collected from the pale-yellow solution by washing and drying it in a vacuum furnace to obtain the CPM powder (Experimental Section in the Supporting Information for details). The CPMs exhibited a high production yield exceeding 70% (**Table S1**). Gram-scale (2.2 g) production was also easily achieved in a single reaction conducted in 25 mL of the solution, indicating the suitability of this process for industrial-scale production. To investigate the size of the structures (CPM-A, B), field emission scanning electron microscopy (FESEM) analyses were performed, and the micrographs show microsphere formation with a smooth surface and diameter in the range of approximately 5-20 µm (**Figures 2a–d** and **Figure S3**). The elemental mapping and EDS spectra of a single CPM-A sample unambiguously confirm the presence of C, O, and N (**Figures 2f-h** and **Figure S4**). During the microwave reaction, diameters up to ~1 µm can be realized as the growth is faster than that in a hydrothermal reaction (**Figure S5**).

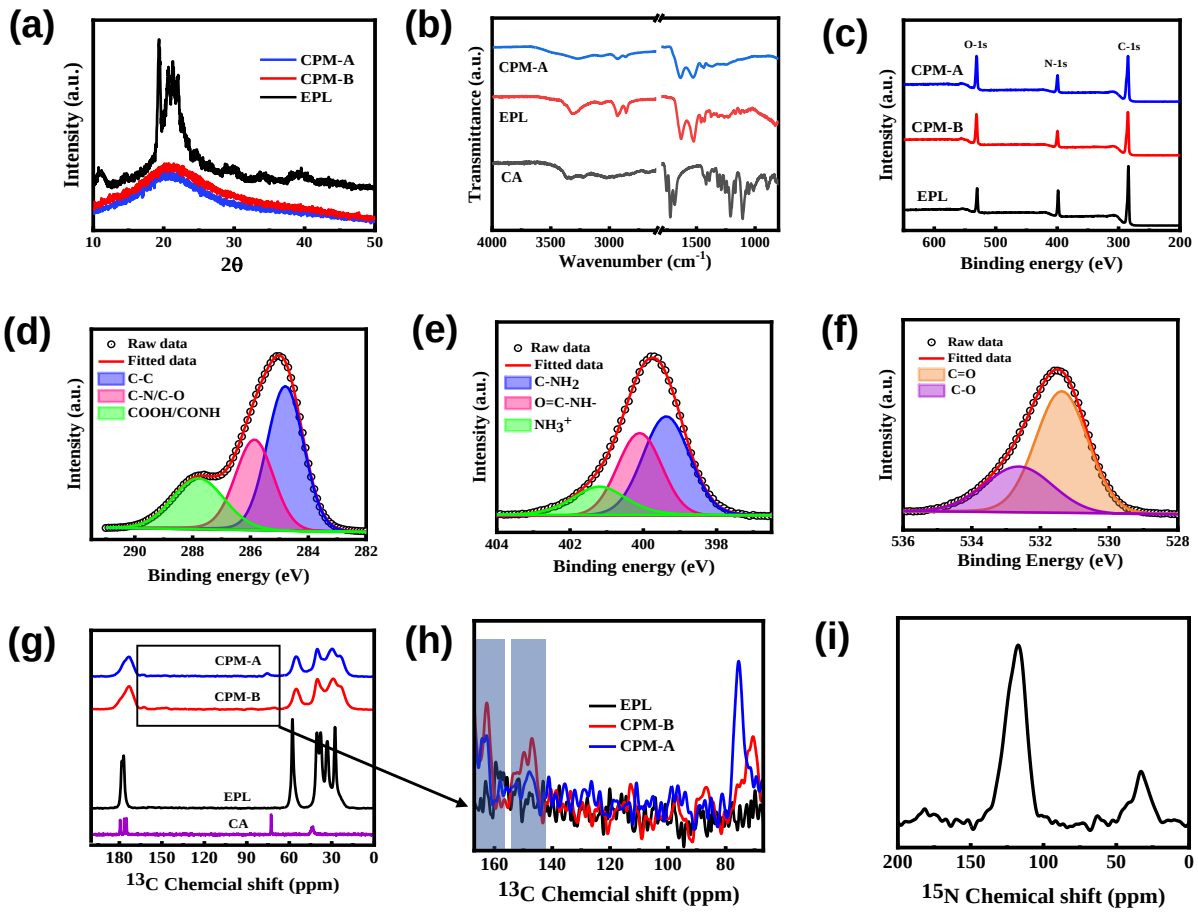

Figure 3. (a-c) XRD, FT-IR, and XPS spectra of EPL and CPM. De-convoluted XPS spectra of (d) C-1s, (e) N-1s, and (f) O-1s of CPM-A. (g-i) Solid-state ^{13}C CP-MAS NMR spectra compared with those of the starting materials CA and EPL, and ^{15}N CPMAS experimental spectra of CPM-A.

Figure 2i shows the typical conversion of CPMs into CPDs. When the -COOH/-NH_2 molar ratio from CA and EPL is approximately 1-1.3, crosslinked microspherical structures are formed (**Figures S6a-c**). However, with a gradual increase in CA, the CPM surface becomes porous, and the CPD structure start to form on the surfaces of the spheres (CPM-C, **Figures S3e and f**). When the -COOH/-NH_2 molar ratio exceeds ~3-5, CPM-aggregates (**Figure S6d**) and water-dispersed CPDs with particle sizes ranging from 5 to 15 nm are formed (**Figures S6e and f**). At 220 °C, aggregated carbonized microstructures with 10-20 nm CPDs are evident (**Figures S7c and d**). This result strongly indicates that the formation of CPM into CPDs is dependent on the reaction conditions. When equal molar ratios of -COOH and -NH_2 are employed, they effectively crosslink to form microspheres. Increasing the reaction temperature and COOH concentration in the reaction medium leads to fragmentation of the chain nano-CPDs formed through EPL **(Figure S8)**. The transmission electron microscopy (TEM) results

in **Figure S9** reveal dark-contrast microspheres, indicating the dense packing of the crosslinked structures. The X-ray diffraction (XRD) patterns show a broad peak at a 2θ value of 21° with the absence of a sharp peak corresponding to EPL, indicating the formation of an amorphous CPM structure (**Figure 3a**).[17, 37, 38] The attenuated total reflection-Fourier transform infrared spectroscopy (ATR-FTIR) spectra reveal that most of the functional groups observed are similar to those of EPL, which indicates that the EPL linear chain structure is aggregated upon its reaction with CA and a microstructure is formed due to the reaction of the functional groups (**Figure 3b**).[39] The X-ray photoelectron spectroscopy (XPS) results in Figure 3c reveal the existence of C, O, and N; where C is the primary component of the CPMs. The N/C ratio of the CPMs gradually decreases from CPM-A to CPM-C compared that of EPL due to crosslinking with CA (**Table S2**), as confirmed by both XPS and CHNO analysis (**Table S3**). The deconvoluted high-resolution XPS (HRXPS) spectrum of CPM-A for C 1s shows different types of C chemical bonding, indicating that various functional groups are present in the CPMs. The C-1s peak of the CPMs mainly consists of three types of C bonds: C-C/C=C, C-N/C-O, and COOH/CONH (**Figure 3d**). The N-1s HRXPS results exhibit a peak at 399.0 eV corresponding to C-NH_2 and C-N-C (pyridinic nitrogen) and a peak at 400 eV due to the amide bond, which demonstrates the formation of a pyridinic bond and a large amide bond (**Figure 3e**).[40-42] In the O 1s region, the two peaks at 531.2 and 532.6 eV attributed to the N-C=O and O-C=O bonds, respectively, are consistent with the different O functionalities of O 1s in the CPMs (**Figure 3f**). The de-convolution of the C-1s, N-1s, and O-1s spectra of CPM-B, C also reveal the presence of different functional groups (**Figure S10**). The CPM structure was characterized by solid-state nuclear magnetic resonance (NMR) using ^{13}C and ^{15}N. The ^{13}C cross-polarization, magic angle spinning (CPMAS) NMR spectra of pure EPL, CA, CPM-A, and CPM-B are presented in **Figure 3g**. The peaks at 179, 176, and 175 ppm from CA and chemical shifts at 178 and 175 ppm correspond to the carboxyl and carbonyl carbons of both CA and EPL.[43] After CPM formation, a broad peak appears at 173 ppm. The signals of the other chain carbons, except Cγ, also show upfield shifts. The C=O C signal of the CPMs is shifted upfield (~3 ppm) compared to that of EPL, suggesting that the α-amino group is protonated by CA. It also reveals a substantial change in the aliphatic C spectral pattern of the CPM compared with that of EPL. The CH_2 sequences in the crystalline component of EPL display a trans-zigzag conformation, resulting in sharp resonances. In contrast, CPM-A and CPM-B exhibit broader resonances than their crystalline components. Both of these upfield chemical shifts and the broadening of the peaks reveal the formation of amorphous CPM via the reaction between EPL and CA.[43-45] The magnified ^{13}C CP-MAS NMR spectra show broad peaks at 162 and 147 ppm.

The small peak at 162 ppm can be assigned to the resonances of C bonded to N. The spectra also exhibit a signal centered at 147 ppm originating from an sp^2-hybridized C not bonded to N. As the chemical shift of this non-protonated C is too low for double bonding to O, this can be a third =C site with -C or -O substitution (**Figure 3h**).[46] These peaks can be attributed to small MF derivatives of 5-oxo-1,2,3,5-tetrahydro-imidazo[1,2-α] pyridine-7-carboxylic acid (IPCA), which are produced and confined in the microstructure via the reaction between CA and EPL. The multi-CP ^{15}N NMR spectrum (**Figure 3i**) exhibits two major distinct peaks at 120 and 33 ppm, attributed to the main ε-NHCO chain and α-NH_3^+ group.[43, 47] Additionally, the CPM shows broad peaks at 33 and 41 ppm, which are related to the ionic bond formation between the ionized carboxylic groups in CA and the α-NH_3^+ group to form the polyionic complex EPL-NH_3^+….$^-$OOC-CA.[45] The small peak centered at 180 ppm corresponds to the formation of an imide bond as an MF structure, which is trapped inside the CPM and is responsible for its optical properties. The thermal gravimetric analysis (TGA) spectrum also confirms that the thermal stability of the CPM is enhanced compared to that of the EPL, which can be attributed to the formation of a crosslinked structure that stabilized the entire CPM (**Figure S11**).

The absorbance spectra of CPM shows peaks at 280 nm and in the range of 340-360 nm tailed with broad visible absorbance. These broad absorbances from the UV region to the high-energy visible light are due to the π–π∗ and n–π* transitions from the entrapped MFs between C-O and C-N bonding configurations (**Figure 4a**). Subsequently, the low-energy absorbance band can be attributed to the n-π* transitions of the cross-linked structures, which included C=O and C=N.[9, 10] Furthermore, theoretical calculations were conducted for possible IPCA derivatives and donor-acceptor molecular conjugated structures using the DFT method at the B3LYP/6-31 G(d, p) level to understand the optical properties.

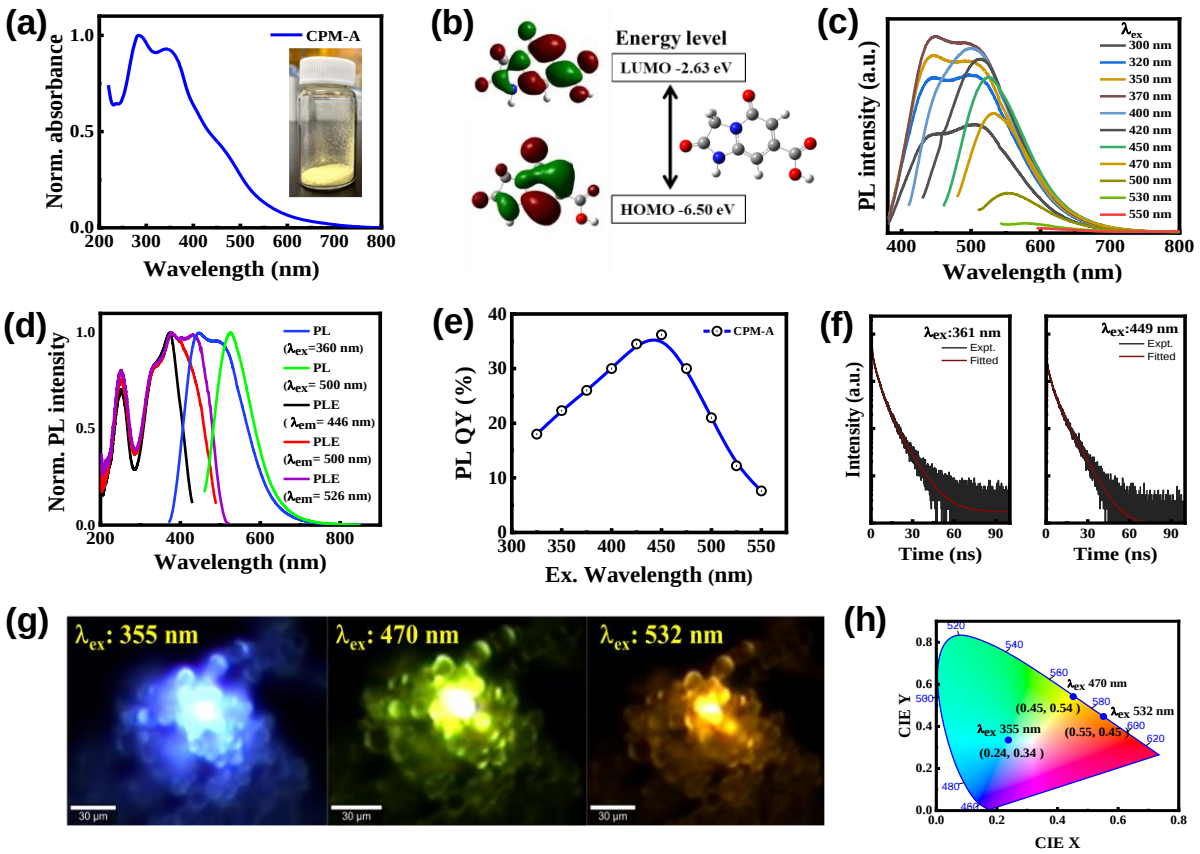

Figure 4. (a) UV-visible spectra of CPM-A (inset shows a photograph). (b) Results of the Gaussian calculation from the optimized IPCA derivate molecules and frontier orbital energy diagram. (c) PL spectra of CPM-A under different excitation wavelengths. (d) Normalized excitation-emission spectra of CPM-A. (e) PLQY at different excitation wavelengths. (f) PL decay curves of CPM-A under 351 and 449 nm excitation and monitored at 449 and 532 nm, respectively. (g) μ-PL image of CPM-A multicolor emission recorded with laser light excitation of 355, 470, and 532 nm. (h) Corresponding CIE coordinates of the multi-color emission of CPM-A.

The LUMO and HOMO energy levels of the structure were calculated to be -2.63 and -6.5 eV, respectively, and their energy gap was 3.87 eV (**Figure 4b**). The simulated absorbance spectra of small MFs of IPCA derivative and corresponding orbital diagrams of HOMO-1 (-7.73 eV) to LUMO (-2.63 eV), indicating the optical energy gap, along with an oscillation stength of f = 0.1292 (**Figure S12**). The predicted absorbance spectra were similar to the experimental results and also showed strong absorption at approximately 347 nm (3.57 eV). The gradual enhancement of the broad absorbance from the UV to visible light range occurred from CPM-A to CPM-C because of the entrapped MF and crosslinking architecture of the

CPMs (**Figure S13**). CPM-A shows excitation wavelength-dependent emission (**Figure 4c**). The emission intensity of the CPMs at longer wavelengths gradually decreases when the excitation wavelength is above 500 nm, which is in accordance with the results of previous studies.[4, 48] Both the PL spectrum and 2D excitation-emission matrix reveal that CPM-A exhibits two major emissions located in the blue and green regions (**Figure S14**). The multi-color emissions ranging from cyan to red wavelengths observed in this system are due to MFs and crosslinked enhancement emissive (CEE) centers embedded within the CPM matrix. These components exist within distinct chemical environments, resulting in complex arrangements of energy levels. When excited at 360 nm, this system produces simultaneous double-peak fluorescence emissions at 446 and 500 nm, resulting in cyan-colored emission. The peak at 446 nm is associated with the presence of IPCA derivatives.[13, 49] The strong emission in the green and higher wavelength region can be attributed to the CEE effect due to amide bond formation.[50, 51] This effect significantly enhances the luminescence of nonconjugated polymer structures by restricting bond vibrations and rotations upon immobilization of small molecular rotors such as –C=N, –C=O, and various hetero-molecules containing double bonds. This restriction of bond movement within the polymer matrix enhances the light emission by increasing the electron concentrations, thus reducing the energy loss through non-radiative pathways. The PL excitation (PLE) spectrum in **Figure 4d** reveals two distinct bands at 251 and 372 nm, aligning with the absorption band of CPM. Notably, the 372 nm bands shift gradually towards the visible light range, forming a new peak at 435 nm when monitored at 500 and 526 nm (**Figure 4d**). The absorption of visible light and prolonged emission in the green wavelength range can be attributed to the formation of interconnected polyamide bonds, resulting in enhanced emission.[10, 52] **Figure 4e** shows the PLQYs of CPM-A under different excitation wavelengths (**Table S4**). Notably, as the excitation wavelength transitions from the UV to blue light range, the PLQY consistently increases, reaching a peak of 36% (λ_{ex} ~ 450 nm), compared to the initial 22% (λ_{ex} ~ 350 nm). **Figure S15** shows the experimental PLQY data for CPM-A, focusing on excitation wavelengths from 350 to 450 nm. The PLQY of CPM gradually decreases owing to the enhancement of MFs in CPM-C, leading to AIQ of CPM (**Figure S16**). The average fluorescence lifetimes (τ_{av}) of CPM-A with 361 and 449 nm excitation are 4.42 and 9.06 ns, respectively (**Table S5**). The broad emission due to UV excitation could be FRET energy transfer from the emitted blue light (λ_{em} ~ 448 nm) originating from the MFs, which is reabsorbed by crosslinked polymeric structures and leads to emission at 500 nm, as evident from τ_{av}. Further reduction of crosslinked amide structures by $NaBH_4$ drastically enhances the PLQY from 23% to 34% (**Figure S17a**) through UV excitation and

emits strong blue light, whereas the 500 nm emission peak intensity decreases and orange emission is suppressed (**Figure S17b, c**). Therefore, τ_{av} of the reduced structures is enhanced from 4.42 ns to 6.91 ns (**Figure S18**), indicating energy transfer from the MFs to crosslinked structures and blue emission (λ_{em} ~ 448 nm) originating from the MF states, whereas green emission is caused by the crosslinked enhanced emission mechanism. The cyan-to-orange multicolor emission in the solid state is also demonstrated as the excitation wavelength varies from 355 nm to 470 and 532 nm, from a consistent position (**Figure 4g**). The micro-photoluminescence (μ-PL) image and spectrum (**Figure S19**) depict cyan, greenish-yellow, and orange emissions emanating from the bulk CPM-A structure. The UV-excited PL spectrum yields Commission Internationale de l'Eclairage (CIE) coordinates of (0.24, 0.35), indicating cyan emission resulting from the combination of blue and green emissions (**Figure 4h**). The materials demonstrate stability in an ambient environment for more than 2 years, with only slight deterioration in their PLQYs. Even under extended exposure to UV-A radiation (365 nm, 4 mW UV power for 7 h), they exhibit robust stability, maintaining a PLQY of approximately 86% (**Figure S20**). The observed decrease in PLQY is ascribed to potential photobleaching. Overall, these CPMs are highly fluorescent in the solid state because of the controlled incorporation of MFs compared to typical non-fluorescent C microspheres, which are hydrothermally derived from glucose, sucrose, etc. (**Figure S21**).

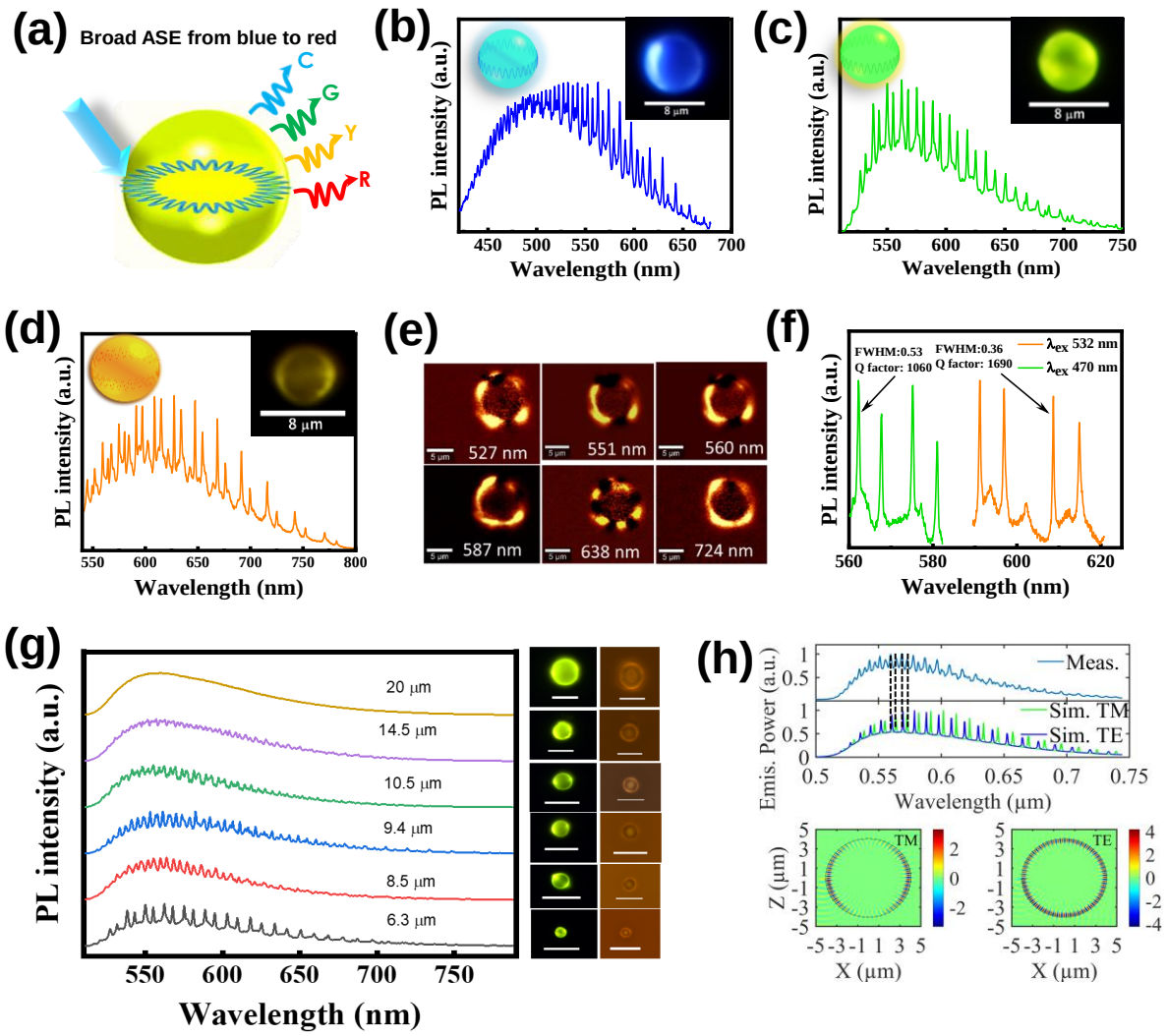

Figure 5. (a) Schematic representation of ASE from blue to red wavelengths. (b–d) WGM emission in the blue–red range from a single CMP via 355, 470, and 532 nm laser excitation on their edge; the inset shows a corresponding PL image of a single CPM and schematic of light confinement. (e) μ-PL mapping image of a single microsphere and corresponding edge light confinement. (f) Q-factor of a CPM via different excitation laser sources. (g) ASE behavior of different-diameter CPMs and corresponding PL images achieved by 470 nm laser edge excitation (scale bar 20 μm). (h) Experimental (top) and simulated (middle) PL spectra excited at 470 nm and E-field distribution (bottom) excited at TM and TE resonances of a single microsphere.

When a single microresonator was excited by a focused laser beam, it formed WGM resonance, and the PL generated inside the sphere was resonantly confined to form standing waves on its surface (**Figure 5a**).[34, 53-55] Because the CPMs exhibit excitation-dependent PL, a

single microsphere can resonate from blue to red by changing the excitation laser (**Figure 5a**). To demonstrate the WGM emission, an experiment was performed using a laser confocal microscope setup with different laser illuminations (355, 470, and 532 nm) at the outer edge of a CPM-A particle (**Figures 5b–d**). During excitation, bright circular cyan, green, and orange PL rings are formed around the circumferences of the particles (**Figures 5b-d**). The PL emission spectra of the same microsphere with different laser excitations display a series of wavelength-dependent intensity modulations with sharp periodic lines in the visible spectrum from 450 to 750 nm, demonstrated as color variable resonance throughout the visible spectram (**Figure S22**). Notably, these modes cannot be excited during the center excitation (**Figure S23**). The WGM emission intensity gradually increases as the laser power increases (**Figure S24**). The edge-excited PL spectrum reveals that the synthesized CPMs have an inbuilt functionality as optical cavities exhibiting tight confinement of the emitted photons within the spherical architecture. Upon excitation, the generated photons are reflected several times via total internal reflection at the microsphere surface, which acted as a high quality-factor (Q-factor) cavity. Thus, WGMs are formed to generate numerous PL waves in constructive interference, yielding several sharp periodic peaks.[35, 56] The single-particle μ-PL mapping also confirms amplified spontaneous emission (ASE) on the edge due to the WGM-assisted light confinement (**Figure 5e**). The efficiency of light confinement by the microresonator was assessed using the Q-factor. For our CPM microresonator, the values of $Q = \lambda/\Delta\lambda$ at 562 and 608 nm are 1060 and 1690 (**Figure 5f**), respectively, where λ is the resonant wavelength and Δλ is the full-width at half-maximum of the resonance, which is superior to the typical π-conjugated polymer sphere, or dye-doped polymer spheres. In general, the Q-factors of WGM resonators can be reduced by external (coupling mechanisms) and internal losses (scattering, absorption, surface contamination...). Here, we utilized relatively low efficiency free-space coupling, which typically presents a coupling efficiency of approximately 30%, resulting in high external losses.[57] Despite these losses, the CPMs display Q-factors as high as ~1690 under 608 nm laser excitation, evidencing a reduced number of internal losses that is attributed to a remarkable smooth surface (**Figures S3a and b**, also proven by the BET study), sphericity, and low absorbance. **Figure 5g** shows the μ-PL spectra of the microspheres with different diameters and their representative optical and μ-PL images. The free spectral range (FSR), which is the difference between two consecutive resonances, is inversely related to the cavity diameter ($FSR = \lambda_m^2/n\pi D$, where n is the refractive index).[58] According to this relationship, upon increasing the diameter of the particles, the FSR gradually decreases with an increase in the number of resonance lines (**Figure S25a**). As the microsphere diameter increases from 6.3 to 20 μm, the

FSR gradually decreases from 13 nm to approximately zero. The WGM resonance and FSR of the large microresonator (diameter > 20 μm) could not be determined due to the rough surface (**Figure 5g**). The microwave-derived CPM diameter is smaller, and an FSR of up to 28 nm can be achieved from a CPM with a diameter of approximately ~ 3 μm (**Figure S25b**), as derived by microwave synthesis. Overall, microsphere diameters below 10 μm show better light confinement owing to the smooth microsphere surface. Conversely, a rough and nanoporous surface leads to the scattering of confined light and a decrease in the Q-factor. To achieve a high Q-factor with CPMs, small-diameter microspheres with smooth surfaces are optimal. Experimental and numerical electromagnetic simulations were performed to verify the photonic properties of the CPM microresonators. The numerical simulation employed the finite-difference time-domain method (Synopsys FullWAVE RSoft). The experimental observations and numerical simulations show the existence of two types of WGMs: transverse magnetic (TM) and transverse electric (TE) (**Figure 5h**). The mode separation of each type of WGM naturally differs owing to the different optical paths, resulting in a collection of resonant peaks spectrally separated in a non-uniform manner. CPM-A exhibits unique excitation-dependent PL (**Figure 4c**); because of this emission property, a single microsphere can emit cyan, green, and orange to red ASE without any chemical modification, which is a distinct advantage from the previously reported conventional π-conjugated polymer-doped synthetic microresonator.

We also successfully demonstrated microcavity-enhanced fluorescence energy transfer for direct WLE, which can be achieved by the direct incorporation of dye molecules during synthesis. Here, the CPMs act as a host matrix for the dye and a fluorescence energy donor. **Figure 6a** presents the absorbance and emission spectra of typical CPM-B and Rhodamine 6G dye (Rh6G) molecules. The PL bands of CPM-B significantly overlap with the absorbance of Rh6G, and light-induced energy transfer from CPM-B to Rh6G is expected. **Figure 6b** shows a digital photograph of dye-incorporated CPMs (CPM@Rh6G1 and CPM@Rh6G2), which were synthesized using Rh6G with concentrations of 0.2 and 1 mM. A distinct change in the color of the material from pale yellow to orange is observed. Upon excitation with UV light, the color changes from cyan to white. The microscopic characterizations reveal similar amorphous microsphere formation during dye doping (**Figure S26**).

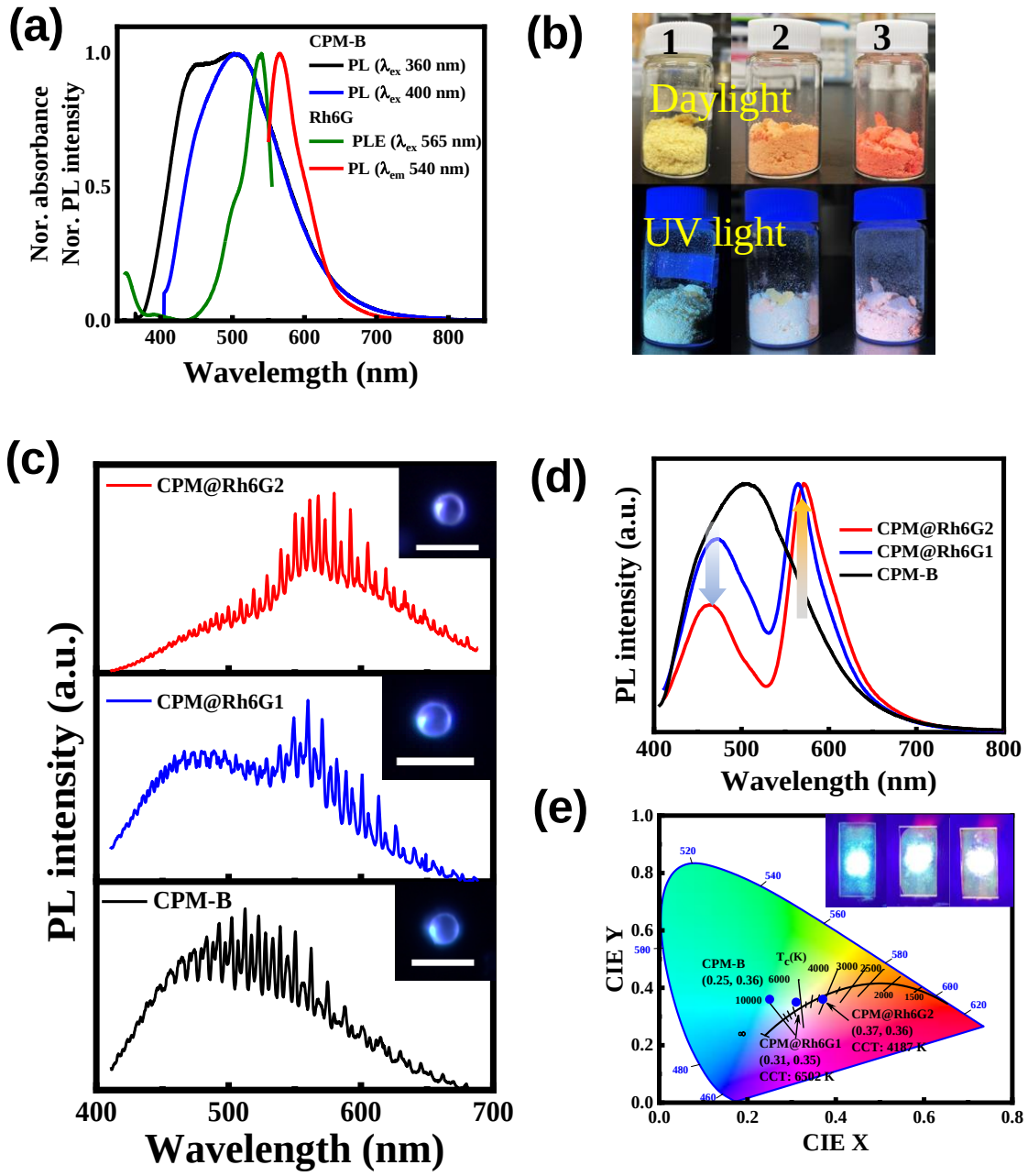

Figure 6. (a) Normalized PL spectra of CPM-B and PLE and PL spectra of Rh6G/PVA film. (b) Photographs of CPM-B- and Rh6G-incorporated microspheres under daylight and UV light. (c and d) WGM emission using 355 nm UV laser excitation and corresponding WLE (scale bar 20 μm). (e) CIE coordinates of WLE. The inset shows a photograph of direct WLE under 400 nm light excitation.

The UV-vis spectra exhibit new absorbance bands at 540 nm, which gradually increase with increasing dye concentration (**Figure S27**). The μ-PL spectra obtained from a single sphere of CPM@Rh6G1, 2 consist of two broad bands at ~470 and 560 nm corresponding to

CPM and Rh6G, respectively (**Figure 6c**). An obvious decrease in the PL emission intensity of the CPM-B, along with an enhancement in the PL band of the dye, are observed. Interestingly, the observed PL spectra also exhibit sharp and periodic lines corresponding to WGM, as the microspheres act as microcavities. The PL spectra cover the entire visible region, from blue to red, and consequently direct WLE is obtained. These observations clearly indicate microcavity-mediated photo-energy transfer via FRET from small MFs inside a microsphere to dyes[34, 59] and that each microsphere can generate WLE (schematic reprenstaion in **Figure S28**). This approach can be very effective in generating WLE for a micropixel array for flat-panel displays with tunable chromaticity. The perimeter and center of a single CPM-B show cyan emission, which gradually transform into the WLE upon dye incorporation (inset of **Figure 6c** and **Figure S29**). To improve understanding of the FRET between CPM and Rh6G, TRPL was investigated at 449 nm excitation. The PL spectrum reveals a noticeable reduction in the emission peak at approximately ~530 nm and an increase in the peak at 570 nm (**Figure S30a**). Before Rh6G dye loading, τ_{av} is 9.1 ns. In the case of 0.2 and 1 mM of dye incorporation, the lifetimes decrease to 7.47 and 6.16 ns, respectively (**Figures S30b and c, Table S6**). Based on these lifetime differences, the energy transfer efficiencies from CPM-B to Rh6G1 on CPM@Rh6G1, 2 are approximately 15% and 29.5%. This finding clearly indicates that the gradual increase in dye loading leads to an increase in the effective excitation energy transfer from CPM to Rh6G.[60] **Figures 6d and e** show the PL spectra and chromaticity diagrams of the CPM-B, CPM@Rh6G1, and CPM@Rh6G2 films. The inset of **Figure 6e** depicts the diffused WLE due to WGM as well as multiple light scattering from the microstructures. The CIE coordinates also vary from (0.25, 0.36) to (0.31, 0.35) and (0.37, 0.36); the corresponding correlated color temperatures are 6502 and 4187 K, with a high color-rendering index (CRI > 80). By simply varying the acceptor dye loading on the microresonator and controlling the FRET process, a single-component WLE with tunable chromaticity can be directly obtained (**Figure S29**). This ability significantly widens the application range and versatility of CPM microresonators, enabling it to cover all the luminescent roles of traditional emitters.

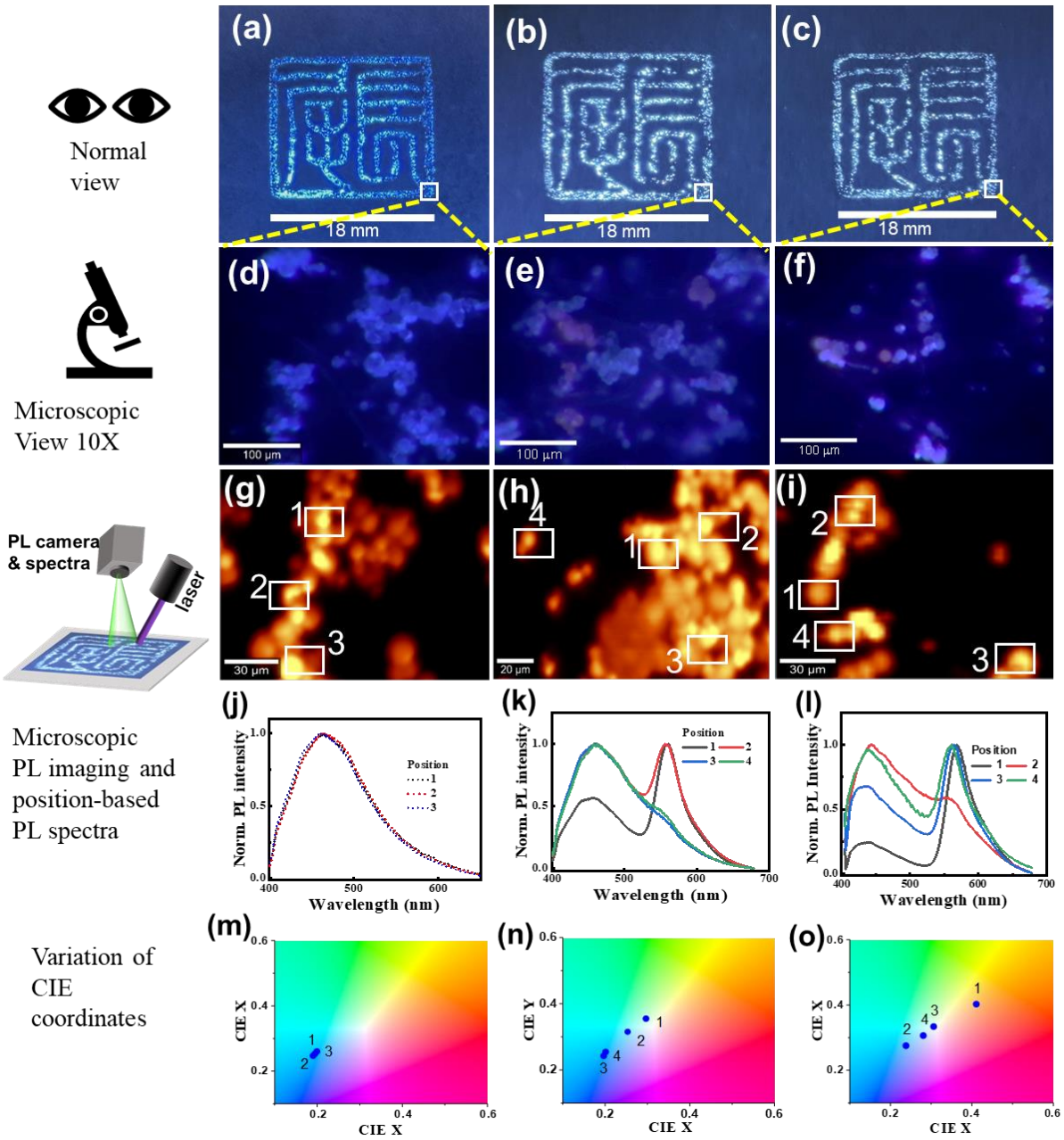

Figure 7. Fluorescence photographs of hanko stamps on white paper using (a) CPM-A and (b) and (c) a mixture of CPM-A+CPM@Rh6G2 ink under UV light. (d–f) enlarged confocal fluoscent microscope images of the white marked regions from the corresponding fluroscent hanko stamps. μ-PL mapping imges of the micro-region hank stamp produced using (g) CPM-A and (h) and (i) CPM-A+CPM@Rh6G2 ink. (j) and (m), (k) and (n), and (l) and (o) μ-PL spectra obtained at and corresponding CIE-coordinates of different positions (white squares) from the μ-PL mapped imges from (g), (h), and (i), respectively.

The unclonable anticounterfeiting application is demonstrated by using these CPM microemitters. Counterfeiting is a major global issue that results in economic losses of trillions

of dollars. Counterfeiters can replicate contract documents, artistic works, electronics, and currency, posing direct threats to economic activity, social well-being, and security.[61-64] Highly protective anticounterfeiting authentication methods such as the use of optically integrated verifiable credentials could be a solution. Because of its color-variable fluorescent and microresonator-based optical response, triply protected unclonable anti-counterfeiting has been demonstrated as a hanko name stamp or an inkan, which is widely used in Eastern and Southern Asia. In this study, three hanko stamps were prepared, one containing CPM-A and two containing a mixture of CPM-A+CPM@Rh6G2 (1:1 wt.%) ink. Upon UV illumination, the CPM-A ink-based hanko stamp emits cyan light (**Figure 7a**), whereas the mixture microsphere ink emits white light (**Figures 7b and c**). The enlarged fluorescence microscope image of CPM-A shows that each microsphere emits cyan light (**Figure 7d**). However, for the stamps containing mixtures of the microspheres inks, the enlarged microscopic images show variations in emission, ranging from cyan to white depending on the presence of CPM-A and CPM@Rh6G2 microspheres (**Figure 7e**). The cyan and white emissions from the microspheres in the stamp vary for each stamp containing the ink consisting of a mixture of microspheres due to their random distribution. Although **Figures 7b and c** both exhibit white light under UV excitation, differences exist in the microscopic fluorescent images because of the random arrangement of two distinct emitting microspheres, as shown in **Figures 7e and f**. Additionally, the microscopic PL mapping, position-dependent spectrum analysis, and corresponding CIE coordinates of CPM-A ink reveal that both the spectrum and CIE coordinates are identical, as shown in **Figures 7g, j, and m.** However, for the stamps containing the ink consisting of a mixture of microspheres, the PL mapping and corresponding position-dependent PL spectra vary between positions, as illustrated in **Figures 7h and k.** Consequently, the CIE coordinates also exhibit variation due to the different PL spectra from the random distribution of CPM-A (blue emission) and CPM@Rh6G2 (white emission), as depicted in **Figure 7n.** Similarly, the PL mapping images and corresponding position-dependent PL spectrum exhibit variations in the case of the second stamp using ink with the same mixture of microspheres, as shown in **Figures 7i and l**. Consequently, the resulting CIE coordinates also differ, as demonstrated in **Figure 7o**. The pattern of the PL spectrum and CIE coordinates differ between stamps prepared from the same ink (**Figures 7k and n** and **Figures 7l and o**), as the microspheres are randomly distributed in each marked stamp, making replication impossible. Furthermore, the spectral patterns of WGM PL in the microresonators vary depending on their diameters. Each microresonator possesses a unique spectral fingerprint. Hence, these microresonators can serve as an exceptionally robust anti-counterfeiting system that is difficult to replicate.[65] The WGM

PL spectral patterns of the two microspheres in a hanko stamp (**Figure 7b**) are different. The spectral patterns of each sphere are distinct and difficult to replicate (**Figure S31**). This anti-counterfeiting strategy incorporates three levels of protection: 1) fluorescence micrographs exhibiting varying emission from two distinct types of microspheres on a macroscopic scale, 2) position-dependent chromaticity, and 3) unique emission spectra at each position of the CPM particles. This anti-counterfeit is not possible with typical CDs or dye-based counterfeit ink because they can be cloned (**Figure S32**). This hierarchically protected unique authentication method can be employed to provide high-level security that is impossible to replicate. This new strategy for unclonable anti-counterfeiting applications involves utilizing the solid-state emission from a mixture of two different types of CPM-based ink. This technique is compared with CND-based anti-counterfeiting in **Table S7**.

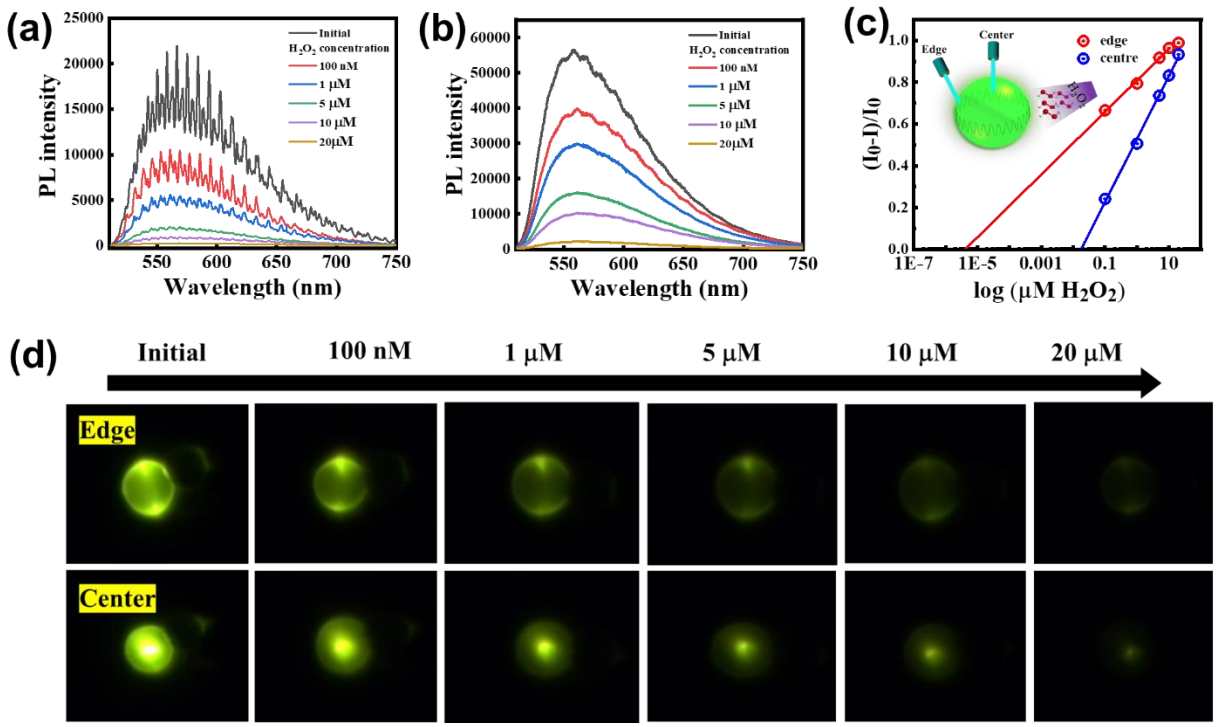

Figure 8. (a) and (b) μ-PL spectrum as H_2O_2 is incrementally added, with laser excitation applied at both the edge and center of the microstructures. (c) Decrease in the PL intensity *vs.* the logarithm of peroxide concentration. (Inset schematically represents the laser excitation on the sphere.) (d) μ-PL images capturing the progression from the initial state to different concentrations of H_2O_2, both on the edge (upper) and center (lower) of the microsphere. The 470 nm pulse laser serves as the excitation light source.

Optical micro-resonators have practical applications in chemical sensing due to the distinct spectral peak patterns observed in their interference. The modulation of PL emission is effective

for chemical sensing purposes.[66-68] This CPM microresonator functions as a single-microparticle-based chemical sensor, particularly for detecting H_2O_2, a crucial component in physiological processes. When exposed to H_2O_2, the surface of CPM-A undergoes gradual oxidation, leading to a rapid decrease in emission intensity. This enables real-time local imaging of chemical reactions with H_2O_2 using a single microsphere. In **Figures 8a and b**, the μ-PL spectrum from a ~9-μm-diameter single microsphere (**Figure S33**) illustrates the reduction in emission intensity as the H_2O_2 solution concentration is incrementally increased from 100 nM to 20 μM. Notably, the decrease in WGM-based emission from the perimeter occurs much faster than that from the center of the sphere. The detection limit of this sensing method reaches as lows as 7 pM (which corresponds to the PL sensitivity limit of $(I_0 - I)/I_0 \approx 0.01$ in **Figure 8c**, edge plot) due to the sharp decline in WGM emission from the chemically modified surface of the microsphere (**Figure 8c**). The corresponding μ-PL images, captured under laser excitation, demonstrate the progression from the initial state to different H_2O_2 concentrations, both at the edge (upper) and center (lower) of the microsphere, showcasing a well-correlated decrease in PL emission intensity with increasing H_2O_2 concentration (**Figure 8d**). This study demonstrates the efficacy of microresonators in chemical sensing compared to conventional emission-based chemical sensors.

3. Conclusion

We successfully developed a novel and versatile solid-state fluorescence microarchitecture based on the integration of photonics and chemical principles that is both robust and naturally inspired and supports a diverse array of optical functionalities. The formation of CPMs is intricately linked to the relative ratios of CA and EPL as well as the specific reaction conditions, which are crucial in shaping both the microstructure and fragmentation of linear polymeric chains. The resulting microresonator structure exhibits a remarkable ASE range, spanning the entire visible spectrum from blue to red, owing to the formation of MFs entrapped within the microspheres. This unique optical property of integrating photonics and chemistry in our single-step synthesis process yields microcavity-enhanced energy transfer, enabling notable achievements such as direct WLE, multilevel anti-counterfeit authentication, and highly sensitive chemical sensing. Notably, the utilization of CPMs circumvents the use of toxic inorganic quantum dots and rare-earth materials and transcends the limitations of conventional CDs and CPDs. The findings of this study not only expand the horizon of integrated photonics and chemistry, but also provide a promising sustainable and efficient alternative to the existing technologies for transformative advancements in a multitude of cutting-edge applications.

4. Experimental Section

Synthesis: CPMs were prepared using EPL from JNC Corporation (Tokyo, Japan), which was a 25% w/v aqueous solution with a molecular weight of approximately 4600 g/mol (36 mer). CA monohydrate was obtained from FUJIFILM Wako Pure Chemical Corporation, and all other reagents were purchased from Wako Pure Chemical Industries (Osaka, Japan) without further purification. To synthesize the CPMs, CA and EPL solutions were mixed in 25 mL of Milli-Q water. The mixture was thoroughly sonicated for approximately 5 minutes and then transferred to a clean autoclave for hydrothermal reaction. After the reaction, a solid yellow CPM precipitated at the bottom of the Teflon container. The solid CPM was washed several times with water and ethanol before being dried in a vacuum furnace at 60°C for 2 h. The hydrothermal synthesis process and the various parameters are detailed in Table S1. In the case of dye-doped CPM, a hydrothermal reaction was conducted by introducing 0.2 mM and 1 mM Rh6G into the reaction medium alongside CA and EPL. Additionally, CPM synthesis was carried out using a microwave synthesizer (Discover from CEM) at 180°C for 25 min with a microwave power of 200 W. The synthesized CPM was utilized for various characterizations and applications.

Characterizations: Various characterization techniques were employed to analyze the microstructure and properties of the materials under investigation. Scanning electron microscopy (SEM) was performed using a Hitachi model SU-8000 FE-SEM and TM3000 table-top SEM-EDX operating at 5-10 kV with Si as the substrate and Pt for coating. TEM images were obtained using an FEI-Tecnai G2 operating at 200 kV on C-coated Cu TEM grids. The crystal properties were determined using XRD with Cu Kα radiation on a RINT Ultima III instrument from Rigaku Corporation. The composition and chemical bonding states were analyzed through CHNO elemental analysis, XPS, solid-state NMR spectroscopy, and ATR-FTIR. For XPS, a PHI Quantera SXM with an Al Kα X-ray source was utilized, and the ATR-FTIR measurements were conducted on a Nicolet iS50 FTIR instrument. Solid-state NMR measurements of 13C and 15N via CPMAS NMR were performed using JEOL/ECA 800 MHz for 13C and JEOL/ECA 500 MHz for 15N.

The UV-VIS absorbance spectra were obtained using a JASCO (V-770) UV−VIS−NIR spectrometer in reflectance mode with an integrating sphere. The PL and PLE spectra of the CPM powder samples were acquired using powder cell holder with a fluorescence spectrometer (JASCO, FP-8650). The spectral correction of the FL spectrum was performed to remove the instrumental function from the measured data. The absolute PLQYs of the CPMs were

determined using a Hamamatsu Photonics K.K. quantum yield measurement system (model C9920-02). This system utilized a Xe lamp for excitation, coupled with a monochromator for precise wavelength control. An integrating sphere served as the sample chamber, and two multi-channel analyzers detected signals within the visible spectrum range. Measurements were conducted in scanning mode, varying the excitation wavelength from 300 to 550 nm in different intervals. The PLQYs were calculated by comparing the reference spectral power density (measured with an empty quartz sample holder) to the sample spectral power density (measured under the same conditions but with the sample present). The software of the system then computed the emission quantum yield based on integration ranges for excitation and emission wavelengths. The fluorescence decay profiles were recorded using a NanoLog time-correlated single photon counting lifetime spectroscopy system from Horiba Jovin Ybon, Japan. The system featured pulsed laser diodes that emitted light at two distinct wavelengths: 361 nm, with an average pulse duration of 1.0 ns or less and a frequency of 1 MHz, and 449 nm, with an average pulse duration of 1.2 ns and a frequency of 1 MHz. These laser diodes functioned as the excitation light source for the experimental procedures. The CPM-A sample was dispersed in an alcohol solution for 5 min. Then, the solution containing microspheres was dropped onto a quartz substrate and dried at 50°C to study the PL of single microspheres. A WITec μ-PL system equipped with a model Alpha 300S microscope, a Princeton Instruments model Action SP2300 monochromator, and an Andor iDus model DU-401A BR-DD-352 CCD camera cooled to –60°C was utilized for this purpose. To study single microspheres, a 50× objective with a numerical aperture (NA) of 0.80 was employed to identify individual microspheres, whereas a 10× objective with an NA of 0.30 was used for bulk microsphere PL and imaging. Different laser sources (355, 470, and 532 nm) were used to photoexcite the perimeter and center of single microspheres under ambient conditions. For the bulk microsphere studies, 1.5 and 5 μW of 355 and 470 nm laser power were utilized. H_2O_2 sensing of single microspheres was conducted on a quartz substrate using a 470 nm laser with 50 μW of power and a 50× objective (NA = 0.80). This process involved gradually adding ~5 μL of H_2O_2 solution of varying concentrations onto the targeted CPM, and μ-PL imaging and spectrum acquisition were performed by accumulating data from the edge and center of the microsphere while maintaining their excitation position. An unclonable anticounterfeit demonstration was carried out by creating a Hinako-stamp from CPM-A and CPM-A+CPM@Rh6G mixture in a polyvinyl alcohol (PVA) polymer solution (25 mg in 0.3 wt.% PVA aqueous solution) on paper. The PL spectrum, PL images, and PL mapping were obtained from the prepared hanko-stamp using a confocal microscope with 365 nm UV light and 355 nm laser excitation.

Computational methods: For the small molecule models, excited-state calculations were conducted with TD-DFT methods using a range of functionals (B3LYP) and basis sets (6-31+G (d, p). For absorption, the structures were firstly optimized with the respective functional in the ground state and the vertical excitation energies were computed with the standard linear-response and adiabatic approximations.

Numerical simulation: To simulate the WGM spectra of the CPM, we used the finite-difference time-domain method with the FullWAVE package from Rsoft by Synopsys. The simulation included a Gaussian source as an excitation and a detector as a monitor, both located at the edge of the sphere. The electric field oscillated along the X-axis and propagated along the –Z-axis, with the incident field amplitude and phase normalized to 1. To ensure accurate results, we applied a perfectly matched layer boundary condition in all directions of the sphere. The refractive index of the CPMs was set to 1.45.

Efficiency of FRET energy transfer: FRET involves energy transfer inversely linked to the sixth power of the distance (r) between donor and acceptor molecules. The efficiency (E_{FRET}) is given by $E_{FRET} = \frac{1}{1+\left(\frac{r}{R_\circ}\right)^6}$, where $R_\circ$ is the characteristic distance for the donor–acceptor pair and E_{FRET} attains a value of 0.5.[69] Experimental detection methods include quenching of donor fluorescence and sensitized acceptor fluorescence.[70] The FRET efficiencies (E) were determined through steady-state measurements: $E = 1 - \frac{\tau_{DA}}{\tau_D}$, where τ_{DA} and τ_D are the donor fluorescence lifetimes in the presence and absence of the acceptor, respectively. This sheds light on the intricate dynamics of molecular-level energy transfer.

ASSOCIATED CONTENT

Supporting Information

The Supporting Information is available free of charge.

Synthesis experimental, condition table, TEM images, SEM images, XPS, HRXPS, PL, UV-VIS, simulated UV-VIS spectra, time-resolved PL spectra, power dependent WGM, individual microspheres WGMs emission, energy transfer, comparison table.

AUTHOR INFORMATION

Corresponding Author

Barun Kumar Barman - International Center for Materials Nanoarchitectonics (WPI-MANA), National Institute for Materials Science (NIMS), Tsukuba, Ibaraki 305-0044, Japan; orcid.org/0000-0002-9894-1890.
Email: BARMAN.Kumarbarun@nims.go.jp

Tadaaki Nagao - International Center for Materials Nanoarchitectonics (WPI-MANA), National Institute for Materials Science (NIMS), Tsukuba, Ibaraki 305-0044, Japan; Department of Condensed Matter Physics, Graduate School of Science, Hokkaido University, Sapporo, Hokkaido 060-0810, Japan; orcid.org/0000-0002-6746-2686.
Email: NAGAO.Tadaaki@nims.go.jp

Authors

Barun Kumar Barman - International Center for Materials Nanoarchitectonics (WPI-MANA), National Institute for Materials Science (NIMS), Tsukuba, Ibaraki 305-0044, Japan; orcid.org/0000-0002-9894-1890

David Hernández-Pinilla- International Center for Materials Nanoarchitectonics (WPI-MANA), National Institute for Materials Science (NIMS), Tsukuba, Ibaraki 305-0044, Japan

Thang Duy Dao-Integrated Photonics Technologies Unit, Microsystems Division, Silicon Austria Labs (SAL), Europastraße 12, 9524 Villach, Austria

Kenzo Deguchi-Solid-State NMR Group, Research Center for Advanced Measurement and Characterization, National Institute for Materials Science, Tsukuba, Ibaraki 305-0003, Japan

Shinobu Ohki- Solid-State NMR Group, Research Center for Advanced Measurement and Characterization, National Institute for Materials Science, Tsukuba, Ibaraki 305-0003, Japan

Kenjiro Hashi- Solid-State NMR Group, Research Center for Advanced Measurement and Characterization, National Institute for Materials Science, Tsukuba, Ibaraki 305-0003, Japan

Atsushi Goto- Solid-State NMR Group, Research Center for Advanced Measurement and Characterization, National Institute for Materials Science, Tsukuba, Ibaraki 305-0003, Japan

Tsuyoshi Miyazaki-First-Principles Simulation Group, Nano-Theory Field, International Center for Materials Nanoarchitectonics (WPI-MANA), National Institute for Materials Science (NIMS), Tsukuba, Ibaraki 305-0044, Japan

Karuna Kar Nanda-Institute of Physics, P. O. Sainik School, Bhubaneswar – 751005, India
Materials Research Centre, Indian Institute of Science, Bangalore – 560012, India
Homi Bhabha National Institute, Anushakti Nagar, Mumbai - 400094, India

Tadaaki Nagao - International Center for Materials Nanoarchitectonics (WPI-MANA), National Institute for Materials Science (NIMS), Tsukuba, Ibaraki 305-0044, Japan; Department of Condensed Matter Physics, Graduate School of Science, Hokkaido University, Sapporo, Hokkaido 060-0810, Japan; orcid.org/0000-0002-6746-2686

Author Contributions

B. K. Barman and T. Nagao conceived and designed the experiments. B. K. Barman carried out most of the experiments. T. D. Dao performed the numerical simulation and modeling. K. Deguchi, S. Ohki, K. Hashi, A. Goto, carried out the solid-state NMR measurements and data analysis. T. Miyazaki support the theoretical calculations. K. K. Nanda discussed the results and commented on the manuscript. B. K. Barman, D. H.-Pinilla, T. D. Dao, and T. Nagao analyzed the data and wrote the manuscript. The manuscript was written through contributions of all authors. All authors have given approval to the final version of the manuscript.

Notes

The authors declare no competing financial interest.

Acknowledgements

This study was supported by the Japanese Society for the Promotion of Science (JSPS) through the KAKENHI program, grant no. 16H0636 and NIMS Quantum Materials Project grant no. AE5010. The BKB also acknowledges the JSPS for their support via a JSPS postdoctoral fellowship for research in Japan. BKB and TN are grateful to the JNC Corporation for discussions and providing the EPL. The authors thank to Dr. H. Yamada for TRPL

measurements. The authors also thanks to Dr. G. Hayase for the BET measurements. The authors thank Ms. K. Okano for technical assistance and the Namiki Foundry at NIMS for the XRD, SEM, TEM, and optical characterizations.

References

1. Miao, X.; Qu, D.; Yang, D.; Nie, B.; Zhao, Y.; Fan, H.; Sun, Z., Synthesis of Carbon Dots with Multiple Color Emission by Controlled Graphitization and Surface Functionalization. *Advanced Materials* **2018,** *30* (1), 1704740.

2. Jiang, K.; Sun, S.; Zhang, L.; Lu, Y.; Wu, A.; Cai, C.; Lin, H., Red, Green, and Blue Luminescence by Carbon Dots: Full-Color Emission Tuning and Multicolor Cellular Imaging. *Angewandte Chemie International Edition* **2015,** *54* (18), 5360-5363.

3. Xia, C.; Zhu, S.; Feng, T.; Yang, M.; Yang, B., Evolution and Synthesis of Carbon Dots: From Carbon Dots to Carbonized Polymer Dots. *Advanced Science* **2019,** *6* (23), 1901316.

4. Sun, Y.-P.; Zhou, B.; Lin, Y.; Wang, W.; Fernando, K. A. S.; Pathak, P.; Meziani, M. J.; Harruff, B. A.; Wang, X.; Wang, H.; Luo, P. G.; Yang, H.; Kose, M. E.; Chen, B.; Veca, L. M.; Xie, S.-Y., Quantum-Sized Carbon Dots for Bright and Colorful Photoluminescence. *Journal of the American Chemical Society* **2006,** *128* (24), 7756-7757.

5. Li, D.; Jing, P.; Sun, L.; An, Y.; Shan, X.; Lu, X.; Zhou, D.; Han, D.; Shen, D.; Zhai, Y.; Qu, S.; Zbořil, R.; Rogach, A. L., Near-Infrared Excitation/Emission and Multiphoton-Induced Fluorescence of Carbon Dots. *Advanced Materials* **2018,** *30* (13), 1705913.

6. Barman, B. K.; Hernández-Pinilla, D.; Cretu, O.; Ohta, R.; Okano, K.; Shiroya, T.; Sasai, J.; Kimoto, K.; Nagao, T., New Insight into Fluorescent Polymeric Carbon Dots for Solid-State Laser Device. *ACS Sustainable Chemistry & Engineering* **2023,** *11* (33), 12291-12303.

7. Holá, K.; Sudolská, M.; Kalytchuk, S.; Nachtigallová, D.; Rogach, A. L.; Otyepka, M.; Zbořil, R., Graphitic Nitrogen Triggers Red Fluorescence in Carbon Dots. *ACS Nano* **2017,** *11* (12), 12402-12410.

8. Lu, S.; Sui, L.; Wu, M.; Zhu, S.; Yong, X.; Yang, B., Graphitic Nitrogen and High-Crystalline Triggered Strong Photoluminescence and Room-Temperature Ferromagnetism in Carbonized Polymer Dots. *Advanced Science* **2019,** *6* (2), 1801192.

9. Rigodanza, F.; Burian, M.; Arcudi, F.; Đorđević, L.; Amenitsch, H.; Prato, M., Snapshots into carbon dots formation through a combined spectroscopic approach. *Nature Communications* **2021,** *12* (1), 2640.

10. Tao, S.; Zhou, C.; Kang, C.; Zhu, S.; Feng, T.; Zhang, S.-T.; Ding, Z.; Zheng, C.; Xia, C.; Yang, B., Confined-domain crosslink-enhanced emission effect in carbonized polymer dots. *Light: Science & Applications* **2022,** *11* (1), 56.

11. Wang, B.; Yu, J.; Sui, L.; Zhu, S.; Tang, Z.; Yang, B.; Lu, S., Rational Design of Multi-Color-Emissive Carbon Dots in a Single Reaction System by Hydrothermal. *Advanced Science* **2021,** *8* (1), 2001453.

12. Fu, M.; Ehrat, F.; Wang, Y.; Milowska, K. Z.; Reckmeier, C.; Rogach, A. L.; Stolarczyk, J. K.; Urban, A. S.; Feldmann, J., Carbon Dots: A Unique Fluorescent Cocktail of Polycyclic Aromatic Hydrocarbons. *Nano Letters* **2015,** *15* (9), 6030-6035.

13. Ehrat, F.; Bhattacharyya, S.; Schneider, J.; Löf, A.; Wyrwich, R.; Rogach, A. L.; Stolarczyk, J. K.; Urban, A. S.; Feldmann, J., Tracking the Source of Carbon Dot Photoluminescence: Aromatic Domains versus Molecular Fluorophores. *Nano Letters* **2017,** *17* (12), 7710-7716.

14. Vallan, L.; Urriolabeitia, E. P.; Ruipérez, F.; Matxain, J. M.; Canton-Vitoria, R.; Tagmatarchis, N.; Benito, A. M.; Maser, W. K., Supramolecular-Enhanced Charge Transfer within Entangled Polyamide Chains as the Origin of the Universal Blue Fluorescence of Polymer Carbon Dots. *Journal of the American Chemical Society* **2018,** *140* (40), 12862-12869.

15. Yang, J.; Guo, L.; Yong, X.; Zhang, T.; Wang, B.; Song, H.; Zhao, Y. S.; Hou, H.; Yang, B.; Ding, J.; Lu, S., Simulating the Structure of Carbon Dots via Crystalline π-Aggregated Organic Nanodots Prepared by Kinetically Trapped Self-Assembly. *Angewandte Chemie International Edition* **2022,** *61* (33), e202207817.

16. Guo, J.; Lu, Y.; Xie, A.-Q.; Li, G.; Liang, Z.-B.; Wang, C.-F.; Yang, X.; Chen, S., Yellow-Emissive Carbon Dots with High Solid-State Photoluminescence. *Advanced Functional Materials* **2022,** *32* (20), 2110393.

17. Zhu, S.; Meng, Q.; Wang, L.; Zhang, J.; Song, Y.; Jin, H.; Zhang, K.; Sun, H.; Wang, H.; Yang, B., Highly Photoluminescent Carbon Dots for Multicolor Patterning, Sensors, and Bioimaging. *Angewandte Chemie International Edition* **2013,** *52* (14), 3953-3957.

18. Yuan, F.; Yuan, T.; Sui, L.; Wang, Z.; Xi, Z.; Li, Y.; Li, X.; Fan, L.; Tan, Z. a.; Chen, A.; Jin, M.; Yang, S., Engineering triangular carbon quantum dots with unprecedented narrow bandwidth emission for multicolored LEDs. *Nature Communications* **2018,** *9* (1), 2249.

19. Kumar Barman, B.; Nagao, T.; Nanda, K. K., Dual roles of a transparent polymer film containing dispersed N-doped carbon dots: A high-efficiency blue light converter and UV screen. *Applied Surface Science* **2020,** *510*, 145405.

20. Ma, P.; Sun, X.; Pan, W.; Yu, G.; Wang, J., Green and Orange Emissive Carbon Dots with High Quantum Yields Dispersed in Matrices for Phosphor-Based White LEDs. *ACS Sustainable Chemistry & Engineering* **2020,** *8* (8), 3151-3161.

21. Chen, Y.; Zheng, M.; Xiao, Y.; Dong, H.; Zhang, H.; Zhuang, J.; Hu, H.; Lei, B.; Liu, Y., A Self-Quenching-Resistant Carbon-Dot Powder with Tunable Solid-State Fluorescence and Construction of Dual-Fluorescence Morphologies for White Light-Emission. *Advanced Materials* **2016,** *28* (2), 312-318.

22. Wu, S.; Shi, H.; Lu, W.; Wei, S.; Shang, H.; Liu, H.; Si, M.; Le, X.; Yin, G.; Theato, P.; Chen, T., Aggregation-Induced Emissive Carbon Dots Gels for Octopus-Inspired Shape/Color Synergistically Adjustable Actuators. *Angewandte Chemie International Edition* **2021,** *60* (40), 21890-21898.

23. Yoo, H. J.; Kwak, B. E.; Kim, D. H., Self-Quenching Origin of Carbon Dots and the Guideline for Their Solid-State Luminescence. *The Journal of Physical Chemistry C* **2019,** *123* (44), 27124-27131.

24. Zhou, D.; Jing, P.; Wang, Y.; Zhai, Y.; Li, D.; Xiong, Y.; Baranov, A. V.; Qu, S.; Rogach, A. L., Carbon dots produced via space-confined vacuum heating: maintaining efficient luminescence in both dispersed and aggregated states. *Nanoscale Horizons* **2019,** *4* (2), 388-395.

25. Meng, T.; Wang, Z.; Yuan, T.; Li, X.; Li, Y.; Zhang, Y.; Fan, L., Gram-Scale Synthesis of Highly Efficient Rare-Earth-Element-Free Red/Green/Blue Solid-State Bandgap Fluorescent Carbon Quantum Rings for White Light-Emitting Diodes. *Angewandte Chemie International Edition* **2021,** *60* (30), 16343-16348.

26. Xu, B.; Li, J.; Zhang, J.; Ning, H.; Fang, X.; Shen, J.; Zhou, H.; Jiang, T.; Gao, Z.; Meng, X.; Wang, Z., Solid-State Fluorescent Carbon Dots with Unprecedented Efficiency from Visible to Near-Infrared Region. *Advanced Science* **2023,** *10* (4), 2205788.

27. Zhang, X.; Yang, H.; Wan, Z.; Su, T.; Zhang, X.; Zhuang, J.; Lei, B.; Liu, Y.; Hu, C., Self-Quenching-Resistant Red Emissive Carbon Dots with High Stability for Warm White Light-Emitting Diodes with a High Color Rendering Index. *Advanced Optical Materials* **2020,** *8* (15), 2000251.

28. Shao, J.; Zhu, S.; Liu, H.; Song, Y.; Tao, S.; Yang, B., Full-Color Emission Polymer Carbon Dots with Quench-Resistant Solid-State Fluorescence. *Advanced Science* **2017,** *4* (12), 1700395.

29. Lu, X.; Rogers, S.; Gerrits, T.; Jiang, W. C.; Nam, S. W.; Lin, Q., Heralding single photons from a high-Q silicon microdisk. *Optica* **2016,** *3* (12), 1331-1338.

30. Vernooy, D. W.; Ilchenko, V. S.; Mabuchi, H.; Streed, E. W.; Kimble, H. J., High-Q measurements of fused-silica microspheres in the near infrared. *Opt. Lett.* **1998,** *23* (4), 247-249.

31. Montanarella, F.; Urbonas, D.; Chadwick, L.; Moerman, P. G.; Baesjou, P. J.; Mahrt, R. F.; van Blaaderen, A.; Stöferle, T.; Vanmaekelbergh, D., Lasing Supraparticles Self-Assembled from Nanocrystals. *ACS Nano* **2018,** *12* (12), 12788-12794.

32. Marino, E.; Bharti, H.; Xu, J.; Kagan, C. R.; Murray, C. B., Nanocrystal Superparticles with Whispering-Gallery Modes Tunable through Chemical and Optical Triggers. *Nano Letters* **2022,** *22* (12), 4765-4773.

33. Vahala, K. J., Optical microcavities. *Nature* **2003,** *424* (6950), 839-846.

34. Okada, D.; Nakamura, T.; Braam, D.; Dao, T. D.; Ishii, S.; Nagao, T.; Lorke, A.; Nabeshima, T.; Yamamoto, Y., Color-Tunable Resonant Photoluminescence and Cavity-Mediated Multistep Energy Transfer Cascade. *ACS Nano* **2016,** *10* (7), 7058-7063.

35. Venkatakrishnarao, D.; Mamonov, E. A.; Murzina, T. V.; Chandrasekar, R., Advanced Organic and Polymer Whispering-Gallery-Mode Microresonators for Enhanced Nonlinear Optical Light. *Advanced Optical Materials* **2018,** *6* (18), 1800343.

36. Chang, J.-W.; Wang, C.-G.; Huang, C.-Y.; Tsai, T.-D.; Guo, T.-F.; Wen, T.-C., Chicken Albumen Dielectrics in Organic Field-Effect Transistors. *Advanced Materials* **2011,** *23* (35), 4077-4081.

37. Kambara, O.; Tamura, A.; Uchino, T.; Yamamoto, K.; Tominaga, K., Terahertz time-domain spectroscopy of poly-L-lysine. *Biopolymers* **2010,** *93* (8), 735-739.

38. Suwalsky, M.; Llanos, A., An X-ray diffraction study of poly(L-lysine hydrobromide). *Biopolymers* **1977,** *16* (2), 403-413.

39. Maeda, S.; Kunimoto, K.-K.; Sasaki, C.; Kuwae, A.; Hanai, K., Characterization of microbial poly (ε-l-lysine) by FT-IR, Raman and solid state 13C NMR spectroscopies. *Journal of Molecular Structure* **2003,** *655* (1), 149-155.

40. Barman, B. K.; Okano, K.; Deguchi, K.; Ohki, S.; Hashi, K.; Goto, A.; Nagao, T., N-Dopant Site Formulation for White-Light-Emitting Carbon Dots with Tunable Chromaticity. *ACS Sustainable Chemistry & Engineering* **2022,** *10* (49), 16136-16149.

41. Ding, H.; Yu, S.-B.; Wei, J.-S.; Xiong, H.-M., Full-Color Light-Emitting Carbon Dots with a Surface-State-Controlled Luminescence Mechanism. *ACS Nano* **2016,** *10* (1), 484-491.

42. Ripalda, J. M.; Román, E.; Díaz, N.; Galán, L.; Montero, I.; Comelli, G.; Baraldi, A.; Lizzit, S.; Goldoni, A.; Paolucci, G., Correlation of x-ray absorption and x-ray photoemission spectroscopies in amorphous carbon nitride. *Physical Review B* **1999,** *60* (6), R3705-R3708.

43. Dos, A.; Schimming, V.; Tosoni, S.; Limbach, H.-H., Acid−Base Interactions and Secondary Structures of Poly-l-Lysine Probed by 15N and 13C Solid State NMR and Ab initio Model Calculations. *The Journal of Physical Chemistry B* **2008,** *112* (49), 15604-15615.

44. Maeda, S.; Fujiwara, Y.; Sasaki, C.; Kunimoto, K.-K., Structural analysis of microbial poly(ε-L-lysine)/poly(acrylic acid) complex by FT-IR, DSC, and solid-state 13C and 15N NMR. *Polymer Journal* **2012,** *44* (2), 200-203.

45. Maeda, S.; Mori, T.; Sasaki, C.; Kunimoto, K.-K.; Kuwae, A.; Hanai, K., Structural investigation of microbial poly(ε-L-lysine) derivatives with azo dyes by solid-state 13C and 15 N NMR. *Polymer Bulletin* **2005,** *53* (4), 259-267.

46. Duan, P.; Zhi, B.; Coburn, L.; Haynes, C. L.; Schmidt-Rohr, K., A molecular fluorophore in citric acid/ethylenediamine carbon dots identified and quantified by multinuclear solid-state nuclear magnetic resonance. *Magnetic Resonance in Chemistry* **2020,** *58* (11), 1130-1138.

47. Dos, A.; Schimming, V.; Chan-Huot, M.; Limbach, H.-H., Effects of hydration on the acid–base interactions and secondary structures of poly-l-lysine probed by 15N and 13C solid state NMR. *Physical Chemistry Chemical Physics* **2010,** *12* (35), 10235-10245.

48. Pan, L.; Sun, S.; Zhang, A.; Jiang, K.; Zhang, L.; Dong, C.; Huang, Q.; Wu, A.; Lin, H., Truly Fluorescent Excitation-Dependent Carbon Dots and Their Applications in Multicolor Cellular Imaging and Multidimensional Sensing. *Advanced Materials* **2015,** *27* (47), 7782-7787.

49. Schneider, J.; Reckmeier, C. J.; Xiong, Y.; von Seckendorff, M.; Susha, A. S.; Kasák, P.; Rogach, A. L., Molecular Fluorescence in Citric Acid-Based Carbon Dots. *The Journal of Physical Chemistry C* **2017,** *121* (3), 2014-2022.

50. Tao, S.; Zhu, S.; Feng, T.; Zheng, C.; Yang, B., Crosslink-Enhanced Emission Effect on Luminescence in Polymers: Advances and Perspectives. *Angewandte Chemie International Edition* **2020,** *59* (25), 9826-9840.

51. Zhu, S.; Wang, L.; Zhou, N.; Zhao, X.; Song, Y.; Maharjan, S.; Zhang, J.; Lu, L.; Wang, H.; Yang, B., The crosslink enhanced emission (CEE) in non-conjugated polymer dots:

from the photoluminescence mechanism to the cellular uptake mechanism and internalization. *Chemical Communications* **2014,** *50* (89), 13845-13848.

52. Zhi, B.; Yao, X.; Wu, M.; Mensch, A.; Cui, Y.; Deng, J.; Duchimaza-Heredia, J. J.; Trerayapiwat, K. J.; Niehaus, T.; Nishimoto, Y.; Frank, B. P.; Zhang, Y.; Lewis, R. E.; Kappel, E. A.; Hamers, R. J.; Fairbrother, H. D.; Orr, G.; Murphy, C. J.; Cui, Q.; Haynes, C. L., Multicolor polymeric carbon dots: synthesis, separation and polyamide-supported molecular fluorescence. *Chemical Science* **2021,** *12* (7), 2441-2455.

53. Kushida, S.; Okabe, S.; Dao, T. D.; Ishii, S.; Nagao, T.; Saeki, A.; Kijima, M.; Yamamoto, Y., Self-assembled polycarbazole microspheres as single-component, white-colour resonant photoemitters. *RSC Advances* **2016,** *6* (58), 52854-52857.

54. Ihara, Y.; Yamagishi, H.; Lin, C.; Jhu, C.-H.; Tsai, M.-C.; Horie, M.; Yamamoto, Y., Hydrothermal crosslinking of poly(fluorenylamine) with styryl side chains to produce insoluble fluorescent microparticles. *Polymer Journal* **2023,** *55* (4), 547-553.

55. Kushida, S.; Braam, D.; Pan, C.; Dao, T. D.; Tabata, K.; Sugiyasu, K.; Takeuchi, M.; Ishii, S.; Nagao, T.; Lorke, A.; Yamamoto, Y., Whispering Gallery Resonance from Self-Assembled Microspheres of Highly Fluorescent Isolated Conjugated Polymers. *Macromolecules* **2015,** *48* (12), 3928-3933.

56. Kushida, S.; Braam, D.; Dao, T. D.; Saito, H.; Shibasaki, K.; Ishii, S.; Nagao, T.; Saeki, A.; Kuwabara, J.; Kanbara, T.; Kijima, M.; Lorke, A.; Yamamoto, Y., Conjugated Polymer Blend Microspheres for Efficient, Long-Range Light Energy Transfer. *ACS Nano* **2016,** *10* (5), 5543-5549.

57. Zhang, Y.; Song, Q.; Zhao, D.; Tang, X.; Zhang, Y.; Liu, Z.; Yuan, L., Review of different coupling methods with whispering gallery mode resonator cavities for sensing. *Optics & Laser Technology* **2023,** *159*, 108955.

58. Anatolii, N. O., Whispering-gallery waves. *Quantum Electronics* **2002,** *32* (5), 377.

59. Jana, S.; Xu, X.; Klymchenko, A.; Reisch, A.; Pons, T., Microcavity-Enhanced Fluorescence Energy Transfer from Quantum Dot Excited Whispering Gallery Modes to Acceptor Dye Nanoparticles. *ACS Nano* **2021,** *15* (1), 1445-1453.

60. Liao, P.; Zang, S.; Wu, T.; Jin, H.; Wang, W.; Huang, J.; Tang, B. Z.; Yan, Y., Generating circularly polarized luminescence from clusterization‐triggered emission using solid phase molecular self-assembly. *Nature Communications* **2021,** *12* (1), 5496.

61. Ma, T.; Li, T.; Zhou, L.; Ma, X.; Yin, J.; Jiang, X., Dynamic wrinkling pattern exhibiting tunable fluorescence for anticounterfeiting applications. *Nature Communications* **2020,** *11* (1), 1811.

62. Pecht, M.; Tiku, S., Bogus: electronic manufacturing and consumers confront a rising tide of counterfeit electronics. *IEEE Spectrum* **2006,** *43* (5), 37-46.

63. Zhang, J.; Liu, Y.; Njel, C.; Ronneberger, S.; Tarakina, N. V.; Loeffler, F. F., An all-in-one nanoprinting approach for the synthesis of a nanofilm library for unclonable anti-counterfeiting applications. *Nature Nanotechnology* **2023**.

64. Maes, R., PUF-Based Entity Identification and Authentication. In *Physically Unclonable Functions: Constructions, Properties and Applications*, Maes, R., Ed. Springer Berlin Heidelberg: Berlin, Heidelberg, 2013; pp 117-141.

65. Okada, D.; Lin, Z.-H.; Huang, J.-S.; Oki, O.; Morimoto, M.; Liu, X.; Minari, T.; Ishii, S.; Nagao, T.; Irie, M.; Yamamoto, Y., Optical microresonator arrays of fluorescence-switchable diarylethenes with unreplicable spectral fingerprints. *Materials Horizons* **2020,** *7* (7), 1801-1808.

66. Yu, D.; Humar, M.; Meserve, K.; Bailey, R. C.; Chormaic, S. N.; Vollmer, F., Whispering-gallery-mode sensors for biological and physical sensing. *Nature Reviews Methods Primers* **2021,** *1* (1), 83.

67. Tanji, N.; Yamagishi, H.; Fujita, K.; Yamamoto, Y., Nanoporous Fluorescent Microresonators for Non-wired Sensing of Volatile Organic Compounds down to the ppb Level. *ACS Applied Polymer Materials* **2022,** *4* (2), 1065-1070.

68. Ngara, Z. S.; Yamamoto, Y., Modulation of Whispering Gallery Modes from Fluorescent Copolymer Microsphere Resonators by Protonation/Deprotonation. *Chemistry Letters* **2019,** *48* (6), 607-610.

69. Förster, T., Zwischenmolekulare Energiewanderung und Fluoreszenz. *Annalen der Physik* **1948,** *437* (1-2), 55-75.

70. Biswas, D. S.; Gaki, P.; Cruz Da Silva, E.; Combes, A.; Reisch, A.; Didier, P.; Klymchenko, A. S., Long-Range Energy Transfer between Dye-Loaded Nanoparticles: Observation and Amplified Detection of Nucleic Acids. *Advanced Materials* **2023,** *35* (29), 2301402.

Synopsis

This study explores carbonized polymer microspheres (CPM) as solid-state micro-photonic emitters, demonstrating adaptable resonant emission across the visible spectrum. Their unique properties offer versatile applications in light emisison, anti-couterfeit, and sensing.

TOC figure